Faraday Discussions

Cite this: *Faraday Discuss.*, 2016, **194**, 117

PAPER

Beyond structure: ultrafast X-ray absorption spectroscopy as a probe of non-adiabatic wavepacket dynamics

Simon P. Neville,[a] Vitali Averbukh,[b] Serguei Patchkovskii,[c] Marco Ruberti,[b] Renjie Yun,[b] Majed Chergui,[d] Albert Stolow*[aef] and Michael S. Schuurman[ae]

Received 4th May 2016, Accepted 7th July 2016
DOI: 10.1039/c6fd00117c

The excited state non-adiabatic dynamics of polyatomic molecules, leading to the coupling of structural and electronic dynamics, is a fundamentally important yet challenging problem for both experiment and theory. Ongoing developments in ultrafast extreme vacuum ultraviolet (XUV) and soft X-ray sources present new probes of coupled electronic-structural dynamics because of their novel and desirable characteristics. As one example, inner-shell spectroscopy offers localized, atom-specific probes of evolving electronic structure and bonding (*via* chemical shifts). In this work, we present the first on-the-fly ultrafast X-ray time-resolved absorption spectrum simulations of excited state wavepacket dynamics: photo-excited ethylene. This was achieved by coupling the *ab initio* multiple spawning (AIMS) method, employing on-the-fly dynamics simulations, with high-level algebraic diagrammatic construction (ADC) X-ray absorption cross-section calculations. Using the excited state dynamics of ethylene as a test case, we assessed the ability of X-ray absorption spectroscopy to project out the electronic character of complex wavepacket dynamics, and evaluated the sensitivity of the calculated spectra to large amplitude nuclear motion. In particular, we demonstrate the pronounced sensitivity of the pre-edge region of the X-ray absorption spectrum to the electronic and structural evolution of the excited-state wavepacket. We conclude that ultrafast time-resolved X-ray absorption spectroscopy may become a powerful tool in the interrogation of excited state non-adiabatic molecular dynamics.

[a]*Department of Chemistry, University of Ottawa, 10 Marie Curie, Ottawa, Ontario, K1N 6N5, Canada. E-mail: albert.stolow@nrc-cnrc.gc.ca*
[b]*Department of Physics, Imperial College London, South Kensington Campus, London, SW7 2AZ, UK*
[c]*Max-Born Institute, Max-Born-Strasse 2A, D-12489 Berlin, Germany*
[d]*École Polytechnique Fédérale de Lausanne, Laboratoire de Spectroscopie Ultrarapide and Lausanne Centre for Ultrafast Science (LACUS), Faculté des Sciences de Base, ISIC, Lausanne CH-1015, Switzerland*
[e]*National Research Council of Canada, 100 Sussex Drive, Ottawa, ON K1A 0R6, Canada*
[f]*Department of Physics, University of Ottawa, 150 Louis Pasteur, Ottawa, ON K1N 6N5, Canada*

1 Introduction

Photo-excited polyatomic molecules often exhibit complex dynamics involving the redistribution of both electronic charge and vibrational energy. Their dynamics are dominated by the non-adiabatic coupling of vibrational and electronic degrees of freedom, typically mediated by conical intersections. These ultrafast excited state processes are variously called radiationless transitions, electronic relaxation or internal conversion and are the primary steps in the photochemistry of many polyatomic molecules as well as photobiological process such as vision and photosynthesis. Ultrafast (femtosecond) pump-probe spectroscopies, wherein an excited state wavepacket is projected onto a set of final states as a function of time, provide powerful and intuitive means by which to study these dynamics with a temporal resolution of the order of the natural timescale for nuclear motion. A pertinent question to ask is how to choose a specific method for a particular problem. For the case of excited state non-adiabatic dynamics, the spectroscopic method should be sensitive to the degrees of freedom under investigation – electronic and vibrational – as well as their coupling. Prominent examples of techniques proposed to address this problem include time-resolved photoelectron spectroscopy (TRPES),[1,2] Time-Resolved High Harmonic Generation (TR-HHG) spectroscopy,[3–5] and two-dimensional electronic spectroscopy.[6,7]

Recent years have seen the development of new ultrafast extreme vacuum ultraviolet (XUV) and X-ray sources, both in laboratories and at large facilities such as synchrotrons and free electron lasers.[8–14] Such sources offer new probes of ultrafast excited state dynamics with desirable characteristics.[15–24] Practical advantages of X-ray probes include high photon energies, which enable the molecule to be probed during all aspects of its dynamics (including dissociation), and the ability to directly obtain structural information from the spectrum. Conceptually, the absorption of XUV and X-ray photons by a molecule results in excitation from core-level orbitals which, unlike the valence-shell excitations probed by UV photons, are highly localized in the vicinity of the nuclei. As such, XUV and X-ray photons offer the unique possibility of atom-specific probes of ultrafast electronic and vibrational dynamics.

The X-ray absorption spectrum is naturally split into two distinct regions: the pre-edge region, corresponding to excitation to quasi-bound core-excited states and the post-edge region, corresponding to direct above-threshold ionization to continuum states. The post-edge part of the spectrum offers a wealth of structural information about bond distances and angles, as well as coordination numbers.[25–28] In a similar vein, ultrafast X-ray scattering has also recently been demonstrated as a powerful probe of structural dynamics following photo-excitation.[29–31] The pre-edge region results from transitions between the core-level orbitals and the bound valence-level orbitals. As such, it provides information about the electronic structure of the initial state.[26,32,33] A key aspect of this paper is the focus on the pre-edge part of the spectrum. The principal reason for doing so is that the dominant core-to-valence transitions embedded in this part of the spectrum are found to be particularly sensitive to the electronic character of the excited-state wavepacket. Motivated by this, and a desire for sensitivity to both electronic and structural dynamics, we present here a theoretical study of the use

of ultrafast pre-edge X-ray absorption spectroscopy in the study of excited state non-adiabatic molecular dynamics.

In this discussion paper, we report time-resolved X-ray absorption spectra (TRXAS) calculated by coupling the *ab initio* multiple spawning (AIMS) method, employing on-the-fly dynamics simulations, with high-level algebraic diagrammatic construction (ADC) X-ray absorption cross-section calculations. An important aspect of the AIMS approach is that it permits not only 'on-the-fly' wavepacket propagation but also 'on-the-fly' calculation of observables which may be directly compared with experiment. To date, the only existing TRXAS calculation is that reported by Penfold *et al.*,[34] who calculated TRXAS spectra for a Cu(I)–phenanthroline complex using a combination of multiconfigurational time-dependent Hartree wavepacket propagations[35,36] and linear-response time-dependent density functional theory (LR-TDDFT) X-ray absorption cross-section calculations. This work highlighted the sensitivity of the TRXAS to the structural dynamics. However, the LR-TDDFT pre-edge spectrum calculations were restricted to a single electronic state. This was due to the restrictions imposed by the LR-TDDFT methodology, which is rigorously valid only for the lowest-lying state of each spin multiplicity. Importantly, by using the ADC method to calculate X-ray absorption cross-sections, we are able to extend the calculation of pre-edge TRXAS spectra to include both ground and excited states.

To proceed, we calculate the dynamics of the fundamental diene, ethylene, following excitation to its optically bright $S_2(\pi\pi^*)$ state. As well as calculating the TRXAS, we also calculate the TRPES using the same quantum dynamics simulations. By doing so, we can compare and contrast the TRXAS, which probes the core-level electrons, to a well established method (TRPES) which probes the valence electrons, and investigate their respective sensitivities to excited state non-adiabatic dynamics. We find that the calculated TRPES and TRXAS contain, in principle, the same information regarding the electronic and structural dynamics. Importantly, however, this information is predicted to be encoded more clearly in the TRXAS, making its interpretation significantly more straightforward.

2 Theory

2.1 Quantum dynamics simulations

We consider a system composed of f nuclear degrees of freedom R_κ and n electronic degrees of freedom r_i. In the AIMS method[37] the ansatz for the total molecular wavefunction $|\Psi(\mathbf{R}, \mathbf{r}, t)\rangle$ reads

$$|\Psi(\mathbf{R}, \mathbf{r}, t)\rangle = \sum_{I=1}^{n_s} \left|\chi^{(I)}(\mathbf{R}, t)\right\rangle |I(\mathbf{r}; \mathbf{R})\rangle. \tag{1}$$

Here, $|\chi^{(I)}\rangle$ denotes the nuclear wavefunction associated with the Ith electronic state $|I\rangle$. The nuclear wavefunctions $|\chi^{(I)}\rangle$ are further expanded in terms of sets of f-dimensional frozen-width Heller-type Gaussian basis functions $\{g_j^{(I)}\}$:

$$\left|\chi^{(I)}(\mathbf{R}, t)\right\rangle = \sum_{j=1}^{N_I} C_j^{(I)}(t) g_j^{(I)}\left(\mathbf{R}; \alpha_j^{(I)}, \overline{\mathbf{R}}_j^{(I)}(t), \overline{\mathbf{P}}_j^{(I)}(t), \gamma_j^{(I)}(t)\right), \tag{2}$$

where $\alpha_j^{(I)}$, $\bar{\mathbf{R}}_j^{(I)}$ and $\bar{\mathbf{P}}_j^{(I)}$ denote, respectively, f-dimensional vectors of the Gaussian widths, positions and momenta associated with each nuclear coordinate R_κ. The positions $\bar{\mathbf{R}}_j^{(I)}$ and momenta $\bar{\mathbf{P}}_j^{(I)}$ are taken to evolve according to classical equations of motion, whilst the phases $\gamma_j^{(I)}$ are propagated semi-classically.[37] The equations of motion for the expansion coefficients $C_j^{(I)}$ are derived variationally *via* the insertion of the wavefunction ansatz 1 into the time-dependent Schrödinger equation. The electronic basis $\{|I\rangle\}$ is chosen as the n_s lowest-lying adiabatic electronic states, and the nuclear coordinates $\mathbf{R}$ are taken as the full set of $3N$ Cartesian coordinates.

The set of Gaussian basis functions $\{g_j^{(I)}\}$ is adaptively increased during the course of the AIMS calculation, in a process termed spawning, so as to be able to describe non-adiabatic transitions between electronic states. Briefly, when a Gaussian basis function $g_j^{(I)}$ enters a region of strong non-adiabatic coupling between the electronic states $|I\rangle$ and $|J\rangle$, additional basis functions $g_j^{(J)}$ are created in the Jth electronic state.[37]

2.2 Calculation of time-resolved photoelectron spectra

We consider ionization from a manifold of N-electron states $|I\rangle$ to a manifold of $(N-1)$-electron states $|\alpha\rangle$. In order to simulate the time-resolved photoelectron spectrum for a given system, we approximate the total photoelectron signal $\sigma(E, t)$ at as an incoherent sum of contributions from the relative probabilities of ionization $W_{I\alpha}$ evaluated at the centres $\bar{\mathbf{R}}_j^{(I)}$ of each Gaussian basis function in the corresponding AIMS calculation:

$$\sigma(E,t) = \sum_{I=1}^{n_s^0} \sum_{\alpha=1}^{n_s^+} \sum_{j=1}^{N_I} \left| C_j^{(I)}(t) \right|^2 W_{I\alpha}\left(\bar{\mathbf{R}}_j^{(I)}(t)\right) \delta\left(E - \left(\omega - \Delta E_I{}^{\alpha}\left(\bar{\mathbf{R}}_j^{(I)}(t)\right)\right)\right), \quad (3)$$

Here, ω is the photon energy of the laser pulse, $\Delta E_I{}^{\alpha}$ is the vertical energy difference between $|I\rangle$ and $|\alpha\rangle$, and n_s^0 and n_s^+ denote the number of neutral and cationic electronic states, respectively. The δ-function arises as we assume vertical ionization. In the case of weak field ionization that is well above the threshold, the squares of the norms of the Dyson orbital $\phi_{I\alpha}^{D}$,

$$\phi_{I\alpha}^{D} = \sqrt{N}\langle I|\alpha\rangle, \quad (4)$$

are qualitative estimates of the relative probabilities of ionization $W_{I\alpha}$,[38] and it is this approach that is taken in this work.

The calculated spectrum is broadened *via* convolution in the time domain using a Gaussian function with a full width at half maximum (FWHM) corresponding to the experimental cross-correlation between the pump and probe laser pulses. Furthermore, in order to account for both the finite widths of the Gaussian basis functions used in the AIMS calculations and the inherent resolution of the experimental spectrum, the calculated spectrum is convoluted in the energy domain using a Gaussian function with a FWHM $\tau \simeq O(10^{-1})$ eV.

It should be emphasized that the observable calculated according to eqn (3) and (4) is only a crude, qualitative estimate of the true TRPES. In particular, it ignores the structure of the continuum, the dipole selection rules, and the inter-channel coupling due to electron correlation. Furthermore, since the nuclear wavepacket amplitudes are accumulated incoherently, it cannot describe the vibrational fine structure of the

spectrum or vibrational wavepacket revivals. In general, the simulated TRPES spectra discussed below would expected to reproduce the central energies and time delays of the major, short-time, features of an experimental spectrum, but not their relative intensities or the detailed, long-time vibrational dynamics.

2.3 Calculation of time-resolved X-ray absorption spectra

We consider core-excitation from a manifold of initial states $\{|I\rangle; I = 1, \ldots, n_s\}$. We approximate the time-resolved X-ray absorption spectrum (TRXAS) $\sigma(E, t)$ as an incoherent sum of contributions calculated at the centres $\bar{\mathbf{R}}_j^{(I)}$ of each Gaussian basis function in the corresponding AIMS calculation:

$$\sigma(E,t) = \sum_{I=1}^{n_s} \sum_{j=1}^{N_I} \left| C_j^{(I)}(t) \right|^2 \sigma_I\left(E; \bar{\mathbf{R}}_j^{(I)}\right). \tag{5}$$

Here, $\sigma_I(E; \mathbf{R})$ denotes the component XAS for the Ith electronic state evaluated at the nuclear geometry $\mathbf{R}$. The component spectra $\sigma_I(E; \mathbf{R})$ are partitioned as follows:

$$\sigma_I(E; \mathbf{R}) = \sigma_I^{(b)}(E; \mathbf{R}) + \sigma_I^{(c)}(E; \mathbf{R}), \tag{6}$$

where $\sigma_I^{(b)}(E; \mathbf{R})$ denotes the part of the XAS arising from excitation into bound core-excited states, whilst $\sigma_I^{(c)}(E; \mathbf{R})$ corresponds to the part arising from core-ionization. Owing to the different normalizations of the final states contributing to $\sigma_I^{(b)}(E; \mathbf{R})$ and $\sigma_I^{(c)}(E; \mathbf{R})$, different methodologies have to be used in their calculation. For the sake of brevity, we give only a brief description here of the methodologies used to calculate the bound and continuum parts of the XAS. A detailed description is given in Appendix B.

The bound part of the spectrum, $\sigma_I^{(b)}(E; \mathbf{R})$, may be calculated simply from the oscillator strengths and excitation energies between the initial valence state and the core-excited states lying below the threshold for core-ionization. On the other hand, the core-excited states lying above the core-ionization threshold cannot be used directly in the calculation of the continuum oscillator strengths required for the construction of the continuum part of the spectrum, $\sigma_I^{(c)}(E; \mathbf{R})$. This is a result of the square-integrable ($\mathscr{L}^2$) Gaussian basis sets employed in our calculations. However, it has long been recognized that the moments of the photoabsorption cross-sections (also termed the spectral moments), $S_I(k) = \langle I|\hat{D}^\dagger \hat{H}^k \hat{D}|I\rangle$, where $\hat{D}$ is the dipole operator, can be accurately calculated using an $\mathscr{L}^2$ basis. The problem of calculating the continuum oscillator strengths can then be reformulated as that of extracting a function from a finite set of its moments. One commonly used solution to this problem is to use a method known as Stieltjes imaging,[39–43] and it is this approach that is used here.

2.4 Electronic structure calculations

In the AIMS simulations, the requisite adiabatic energies, energy gradients, and non-adiabatic coupling terms were evaluated at the multi-reference first-order configuration interaction (MR-FOCI) level. The underlying reference functions were taken as complete active space self-consistent field (CASSCF) wavefunctions constructed using an active space consisting of the π, π^* and Rydberg 3s orbitals,

with state averaging over six states. We denote this level of calculation by MR-FOCI(2,3). Generally contracted basis sets of the atomic natural orbital type[44] obtained from the C(10s6p3s)/H(7s3p) primitive sets with the C[3s2p1d]/H[2s1p] contraction schemes were used. In order to satisfactorily describe the low-lying π3s state, a single additional s function contracted from a set of 8s primitive functions was added to the basis, placed at the centre of mass. The additional diffuse s function was constructed using the procedure detailed in ref. 45. We denote this basis by ANO(3s2p1d/2s1p/1s). Further details of the AIMS simulations (including basis information and initial conditions) are given in Appendix E.

The calculation of the TRXAS was performed using the second-order algebraic diagrammatic construction (ADC(2)) method.[46,47] For the calculation of the initial valence excited states $|I\rangle$, the original strict variant of the ADC(2) method was used. For the calculation of the final, core-excited states $|\mathrm{J}\rangle$, the extended ADC(2) method was used within the core–valence separation approximation,[48] and this level of theory is denoted here by CVS-ADC(2)x. The bound part of the spectrum was calculated using the 6-311++G** basis. The continuum part of the spectrum was calculated using the cc-pVDZ basis augmented with 3s, 6p and 4d uncontracted continuum-type diffuse functions of the Kauffmann–Baumeister–Jungen (KBJ) type[49] placed at the centre of mass. The spectral moments $S_I(k)$ used in the Stieltjes imaging procedure we generated using the block-Lanczos pseudo-spectrum of the CVS-ADC(2)x Hamiltonian.[41–43] TRPES were calculated using Dyson orbitals and vertical ionization energies calculated at the ADC(2) level of theory using the 6-311++G** basis. The details of these calculations are given in Appendix C. The selection of the initial ADC(2) states used in the TRXAS and TRPES calculations was based on a criterion of maximum overlap with the MR-FOCI states of the AIMS calculations, and details of the procedure used are given in Appendix D.

All MR-FOCI calculations were performed using the COLUMBUS set of programs.[50] The canonical Hartree–Fock orbitals used in the ADC calculations were calculated using the GAMESS program.[51] The AIMS calculations were performed using the FMS90 program.

In order to help identify features in the calculated time-resolved spectra attributable to the population of the π3s Rydberg state, further AIMS simulations were run in which the 3s Rydberg orbital was removed from the CASSCF active space. This eliminates the π3s Rydberg state from the AIMS calculation, and also from any TRXAS and TRPES calculation using the thus obtained nuclear densities. We refer to these calculations as the valence-state-only calculations throughout.

2.5 Analysis of the nuclear wavefunctions

In order to analyze the regions of nuclear configuration space sampled by the evolving wavepacket, a useful quantity to calculate is the one-dimensional reduced density $\rho(s, t)$ defined with respect to a given nuclear degree of freedom s:

$$\rho(s,t) = \int \left|\Psi(\mathbf{R},t)\right|^2 \delta\left(f^{(s)}(\mathbf{R}) - s\right) \mathrm{d}\mathbf{R}, \tag{7}$$

where $f^{(s)}(\mathbf{R})$ denotes the function $f^{(s)}$: $\mathbf{R} \rightarrow s$. Following on from the work of Mori *et al.*,[52] we chose to focus on the twisting angle ψ about the C–C bond and the

pyramidalization angle ζ defined with respect to the CH_2 groups. The reason for this choice lies in the fact that internal conversion from the $\pi\pi^*$ state to the ground state of ethylene is known to be facilitated predominantly by a conical intersection (CI) involving large amplitude motion about these two degrees of freedom, the so-called twisted-pyramidalized (Tw-Py) CI.[52,53] With reference to the atom numbering shown in Fig. 1, we note that the angles ψ and ζ are defined as follows:

$$\psi = \cos^{-1}[(\mathbf{r}_{12} \times \mathbf{r}_{34}) \cdot (\mathbf{r}_{21} \times \mathbf{r}_{56})] \tag{8}$$

$$\zeta = \max\{\cos^{-1}[(\mathbf{r}_{12} \times \mathbf{r}_{34}) \cdot (\mathbf{r}_{14} \times \mathbf{r}_{13})], \cos^{-1}[(\mathbf{r}_{21} \times \mathbf{r}_{56}) \cdot (\mathbf{r}_{26} \times \mathbf{r}_{25})]\} \tag{9}$$

Additionally, by choosing s to correspond to the distance to a given CI seam (in the Euclidean sense), information regarding the role played by that seam in the excited state dynamics of a molecule may be assessed. To do so, we take s to be defined as the projection onto the branching space of the distance to the minimum energy conical intersection (MECI) geometry $\mathbf{R}_{\mathrm{MECI}}$ between the electronic states $|I\rangle$ and $|J\rangle$ on the seam of interest. We term this quantity the first-order seam distance, and denote it by $D_{IJ}(\mathbf{R}; \mathbf{R}_{\mathrm{MECI}})$. A description of the procedure used to calculate $D_{IJ}(\mathbf{R}; \mathbf{R}_{\mathrm{MECI}})$ is given in Appendix A.

All reduced densities $\rho(s, t)$ were evaluated using a Monte-Carlo procedure, the details of which have been described previously.[54]

3 Results

3.1 Validation of the X-ray absorption cross-section calculations

Before considering the results of the dynamics and spectroscopic calculations, we begin with a validation of our CVS-ADC(2) X-ray absorption cross-section calculations. To do so, we consider the comparison of the calculated ground state X-ray absorption spectrum (XAS) to its experimental counterpart, as shown in Fig. 2. The calculated and experimental spectra are found to be in good qualitative agreement, both in terms of absolute intensities and peak positions. It should be noted that the moderate disagreement between the calculated and experimental cross-sections at higher energies are a result of the relatively small basis set used in the calculation of the continuum part of the spectrum, necessitated by the very large number of cross-section calculations required for the computation of the TRXAS. Nonetheless, the agreement between the experimental and calculated spectra is sufficient for the purposes of the calculation of a qualitatively correct TRXAS, allowing us to evaluate the utility of this measure for probing ultrafast non-adiabatic dynamics.

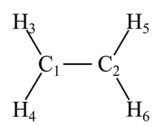

Fig. 1 Atom numbering used in the definition of the twisting angle ψ and the pyramidalization angle ζ.

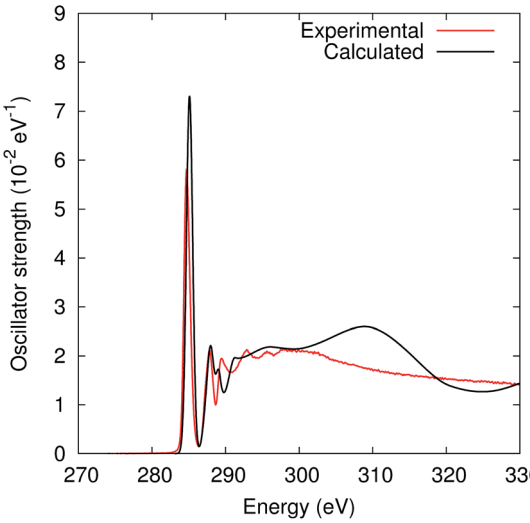

Fig. 2 Experimental[67] and calculated C 1s X-ray absorption spectra for the S_0 state ethylene. The bound part of the calculated spectrum was computed using oscillator strengths and excitation energies calculated at the CVS-ADC(2)x/6-311++G** level of theory. The continuum part was calculated from 20th-order Stieltjes imaging calculation employing spectral moments calculated at the CVS-ADC(2)x/cc_pVDZ/3s6p4d level of theory.

3.2 Dynamics

Previous experimental and computational studies of the dynamics of ethylene following excitation to the optically bright $S_2(\pi\pi^*)$ state exist.[52,53,55–57] The picture emerging from these studies is one of ultrafast internal conversion to the ground electronic state on a sub-100 fs timescale. Previous calculations[52,53] implicated the role of three conical intersections in facilitating internal conversion between the $\pi\pi^*$ and ground states: the twisted-pyramidalized(Tw-Py), ethylidene-type (Et) and hydrogen-bridge (H-br) intersections. The geometries of these conical intersections are shown in Fig. 3. As well as internal conversion to the ground state, a number of previous studies have also suggested that the $S_1(\pi 3s)$ Rydberg state is transiently populated following excitation to the $S_2(\pi\pi^*)$ state: namely, the TRPES study of Champenois *et al.*[56] and the AIMS calculations of Mori *et al.*[52] Our results are found to be in close agreement with this picture and, as such, we present only a brief outline of the most pertinent aspects of our excited state dynamics calculations.

Shown in Fig. 4(a) are the adiabatic state populations calculated following excitation to the $S_2(\pi\pi^*)$ state. Rapid depopulation of the S_2 state is predicted to occur, with 65% of the population of this state being transferred to the S_1 state within 10 fs. Population of the S_1 state is found to reach its maximum at around 25 fs, whereafter internal conversion to the ground state is predicted to occur on a timescale of around 95 fs (determined *via* fitting of a single exponential to the S_0 state population).

In order to reveal which conical intersection seams dominate internal conversion to the ground state, we determined the minimum root mean square

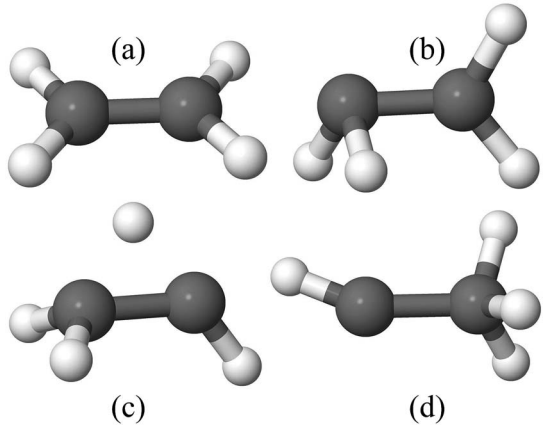

Fig. 3 Geometries of critical points on the S_0/S_1 PESs of ethylene. (a) FC point geometry, (b) Tw-Py MECI, (c) H-br MECI, and (d) Et MECI. All conical intersection geometries were optimized at the MR-FOCI(2,3)/ANO(3s2p1d/2s1p/1s) level of theory.

deviation (RMSD) of each spawn geometry to the ground state from each of the Tw-Py, Et and H-br CI geometries subject to centre of mass translations, rotations and the permutation of identical nuclei. We found that 74% of the spawn geometries map onto the Tw-Py geometry, 4% onto the Et geometry, and 22% onto the H-br geometry. This implies that internal conversion to the ground state *via* the Tw-Py intersection is dominant, in agreement with previous work.[52] As such, we concentrate only on the role played by the Tw-Py conical intersection in the following sections. For reference, the calculated reduced densities for the twisting and pyramidalization angles are shown in Fig. 5(a) and (b), respectively.

Finally, we briefly consider the results of the valence-state-only AIMS calculations, from which the π3s state was excluded. The adiabatic state populations calculated from the valence-state-only AIMS calculations are shown in Fig. 4(b). The time-scale for re-population of the S_0 state is not significantly altered by the exclusion of the π3s state. Additionally, the minimized RMSDs of the spawn-geometries from the Tw-Py, Et and H-br CI geometries are also found to not be significantly altered by the removal of the π3s state, with 78% of the spawn geometries mapping onto the Tw-Py geometry, 1% onto the Et geometry, and 21% onto the H-br geometry. This implies that the removal of the π3s Rydberg state does not significantly affect the excited-state nuclear dynamics. Therefore a meaningful comparison of time-resolved spectra calculated from the AIMS simulations performed with and without the inclusion of the π3s Rydberg state may be made, allowing us to determine the effect of the population of this state on the calculated spectra.

3.3 Time-resolved X-ray absorption spectra

Shown in Fig. 6 is the TRXAS calculated from the AIMS simulations of ethylene following excitation to the $S_2(\pi\pi^*)$ state. For reference, the bound and continuum contributions of the spectrum are shown separately alongside. It is found that the bound part of the TRXAS contains a large amount of structure. In comparison, the

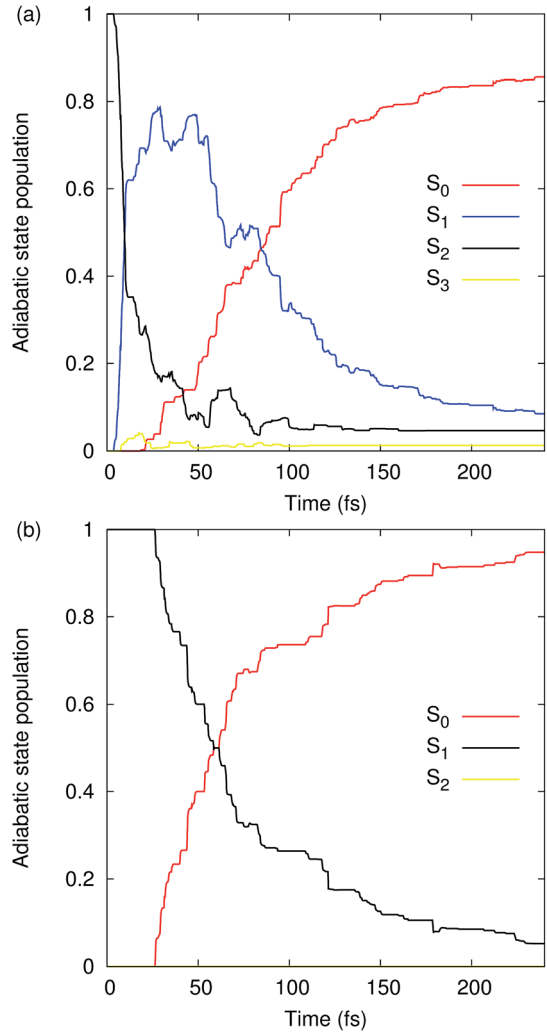

Fig. 4 Adiabatic state populations calculated following excitation to the ππ* state of ethylene. (a) Populations calculated from the all-state AIMS simulation. (b) Populations calculated from the valence-state-only AIMS simulation.

continuum part of the TRXAS is found to be relatively featureless, containing a single, decaying dominant peak. As such, we choose to focus our analysis on the bound part of the TRXAS.

In the following discussion, we consider separately the contributions to the pre-edge TRXAS arising from the dynamics in: (i) the initially excited ππ* state; (ii) internal conversion to the π3s state, and; (iii) the re-population of the ground state.

3.3.1 Dynamics in the ππ* state. At time $t = 0$, the pre-edge part of the TRXAS contains a single, weak peak centred at around 277 eV. At this time, the vertically excited wavepacket is localized around the FC point. In Fig. 7 we show the static X-ray absorption spectrum (XAS) calculated for the S_0, $S_1(\pi 3s)$ and $S_2(\pi\pi^*)$ states

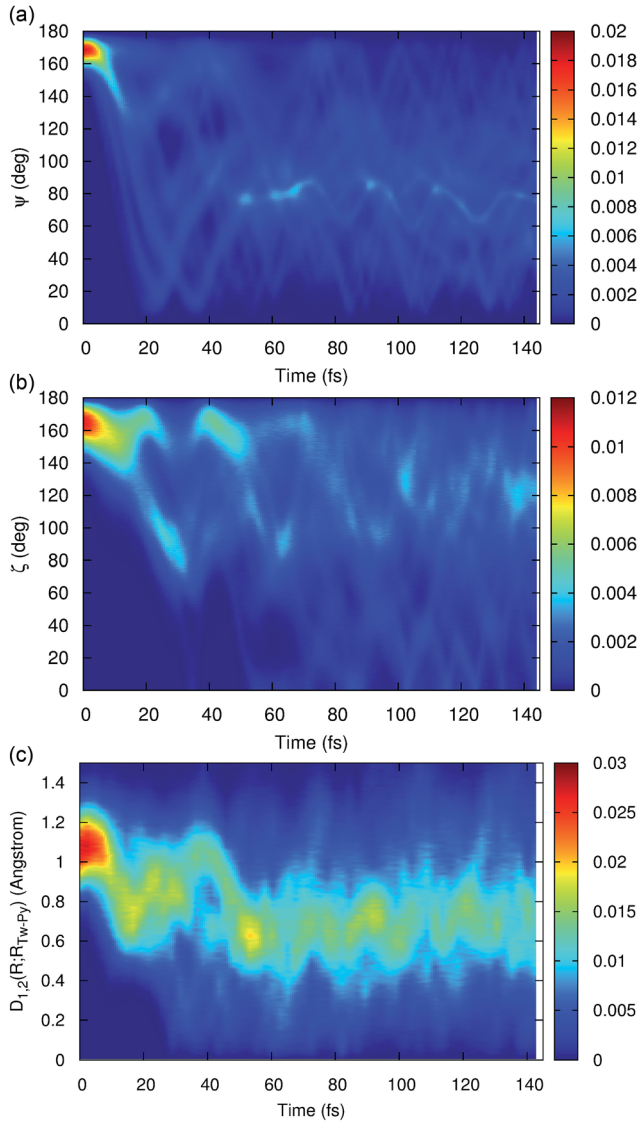

Fig. 5 One-dimensional reduced densities for the twisting angle ψ, the pyramidalization angle ζ, and the distance within the branching space to the Tw-Py conical intersection $D_{1,2}(\mathbf{R}; \mathbf{R}_{\text{Tw-Py}})$, calculated following excitation to the $\pi\pi^*$ state.

at the FC point. Below the core-ionization threshold, the FC point $S_2(\pi\pi^*)$ state XAS is predicted to be dominated by a single, weak peak at around 277 eV. Analysis of the CVS-ADC(2)x wavefunction of the corresponding final core-excited state reveals that this transition corresponds mainly to excitation of a C 1s electron into the hole in the singly-occupied π orbital of the initial $S_2(\pi\pi^*)$ state, forming the $1s\pi^*$ state. As such, it is trivial to assign the bound part of the TRXAS at $t = 0$ to excitation of a core-electron into the singly-occupied π orbital of the initially excited state. We note that this peak rapidly sweeps to higher energies

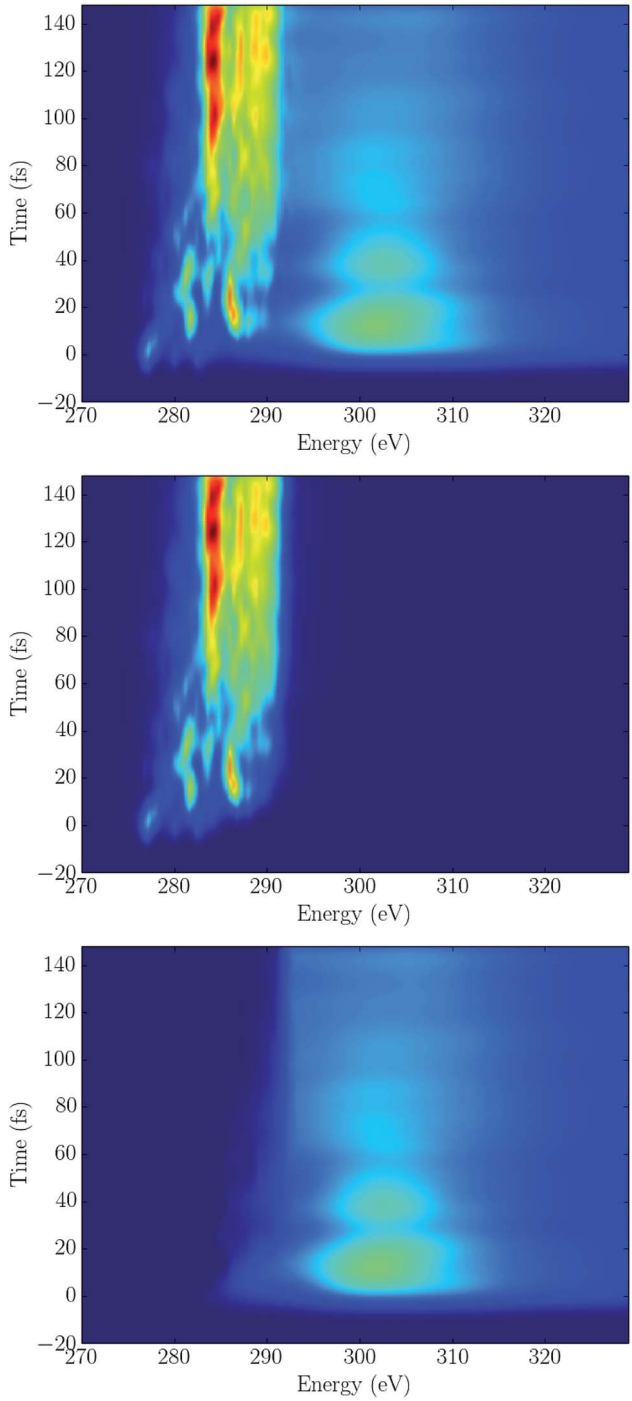

Fig. 6 Calculated TRXAS spectra for ethylene following excitation to the ππ* state. Top: Total TRXAS spectrum. Middle: Bound part of the TRXAS spectrum. Bottom: Continuum part of the TRXAS spectrum.

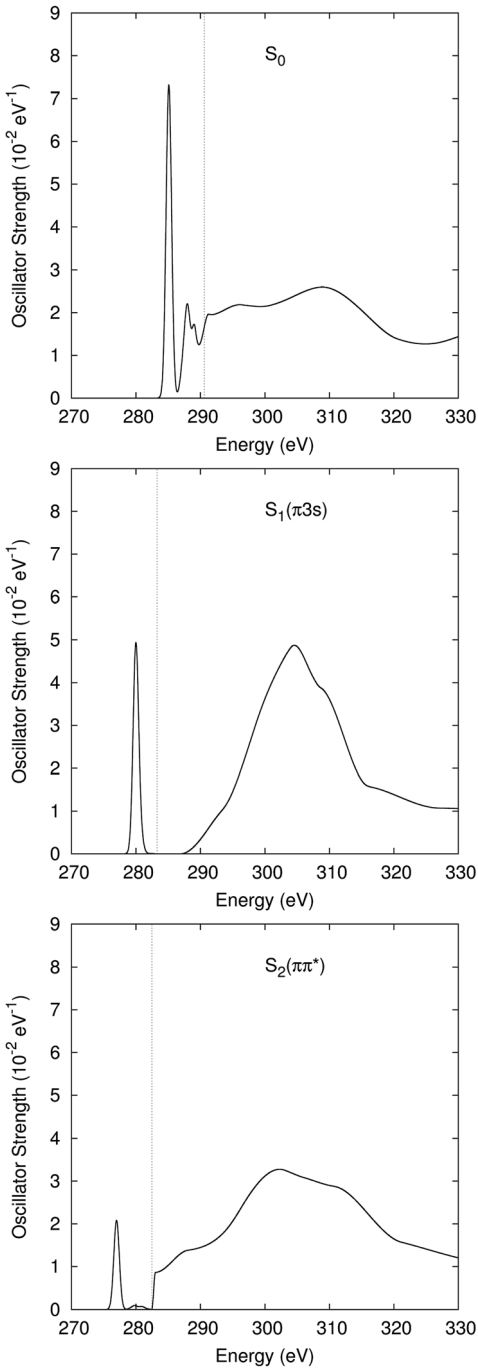

Fig. 7 Calculated XAS for the ground (π^2), $\pi 3s$ and $\pi\pi^*$ states of ethylene at the FC point. The initial valence-excited states were described at the ADC(2) level, and the final core-excited states at the CVS-ADC(2)x level. The dashed lines mark the calculated C 1s ionization energy. The bound-parts of each spectrum were calculated using the 6-311++G** basis. The continuum parts were calculated using the Stieltjes imaging technique with the cc-pVDZ basis augmented with 3s, 6p and 4d continuum-type KBJ functions.

with increasing time. This is a result of rapid twisting about the C–C bond, as corroborated by the calculated reduced densities for the twisting angle ψ shown in Fig. 5(a). The $\pi\pi^*$ potential energy surface (PES) has negative curvature with respect to this degree of freedom, whilst the corresponding curvature of the $1s\pi^*$ state is positive. As such, a rapid increase (sweep) in the vertical excitation energy between the two states accompanies twisting about the C–C bond.

We next consider the peak at around 286 eV in the TRXAS, which develops intensity after ~20 fs. In Fig. 8(b) we show the TRXAS calculated from the valence-state-only AIMS calculations, in which the π3s state is removed. This valence-state-only TRXAS is also found to contain a similarly intense peak at around 286 eV, implying that this peak is not attributable to population of the π3s state. Additionally, no significant population of the ground electronic state is found to occur at this time (see Fig. 4(a)). Therefore, this feature must be attributable to core-excitation from the valence $\pi\pi^*$ state. The timescale for the growth in the intensity of this peak is comparable to the timescale for the movement of the wavepacket to regions of nuclear configuration space proximate to the Tw-Py intersection seam, as illustrated by the reduced densities $\rho(D_{1,2}(\mathbf{R}; \mathbf{R}_{\text{Tw-Py}}))$ shown in Fig. 5(c). Shown in Fig. 8(c) is the pre-edge part of the TRXAS calculated from the valence-only AIMS calculations, but with the removal of all contributions from Gaussian basis functions $g_j^{(I)}$ in the S_1 state for which the distance $D_{12}(\mathbf{R}_j^{(I)}; \mathbf{R}_{\text{Tw-Py}})$ from the Gaussian centre to the Tw-Py intersection seam is less than 0.3 Å. The effect of the removal of these basis functions is to significantly reduce the intensity of the TRXAS in the vicinity of the peak of interest at 286 eV. This strongly suggests that this peak arises from the components of the wavepacket approaching the vicinity of the intersection seam characterized by the Tw-Py CI. Importantly, this observation indicates that TRXAS may – perhaps uniquely – be able to directly observe the approach of a wavepacket to a conical intersection.

3.3.2 Internal conversion to the π3s state. Rapidly, at a time of $t = 10$ fs, a relatively intense new feature in the TRXAS appears at an energy of around 281 eV. This peak is centred very closely to the dominant peak in the calculated FC point pre-edge XAS of the $S_1(\pi 3s)$ state, corresponding again to excitation of a core-electron into the singly-occupied π orbital of the $S_1(\pi 3s)$ state. Additionally, the time at which this feature in the TRXAS appears is concomitant with the calculated timescale for internal conversion to the S_1 state (see Fig. 4(a)), which contains components of both π3s and $\pi\pi^*$ character. Therefore, we assign this feature in the TRXAS to core-excitation from the π3s state following internal conversion from the initially excited $\pi\pi^*$ state. In order to confirm this assignment, the bound part of the TRXAS was re-calculated using nuclear densities from the valence-state-only AIMS calculation. The resulting spectrum is shown in Fig. 8(b). The TRXAS derived from this valence-state-only calculation is similar to the TRXAS derived from the AIMS calculation including the π3s Rydberg state (shown alongside in Fig. 8(a) for comparison), but the relatively intense peak at 281 eV is now missing. This demonstrates that this peak corresponds to excitation from the π3s state.

3.3.3 Internal conversion to the ground state. Finally, we consider the broad, intense pre-edge feature in the TRXAS that appears at a time of $t \sim 50$ fs. This part of the TRXAS comprises three dominant peaks of decreasing intensity centred around 284, 287 and 289 eV. With reference to Fig. 7, we note that these positions match those of the dominant pre-edge transitions in the calculated FC point XAS

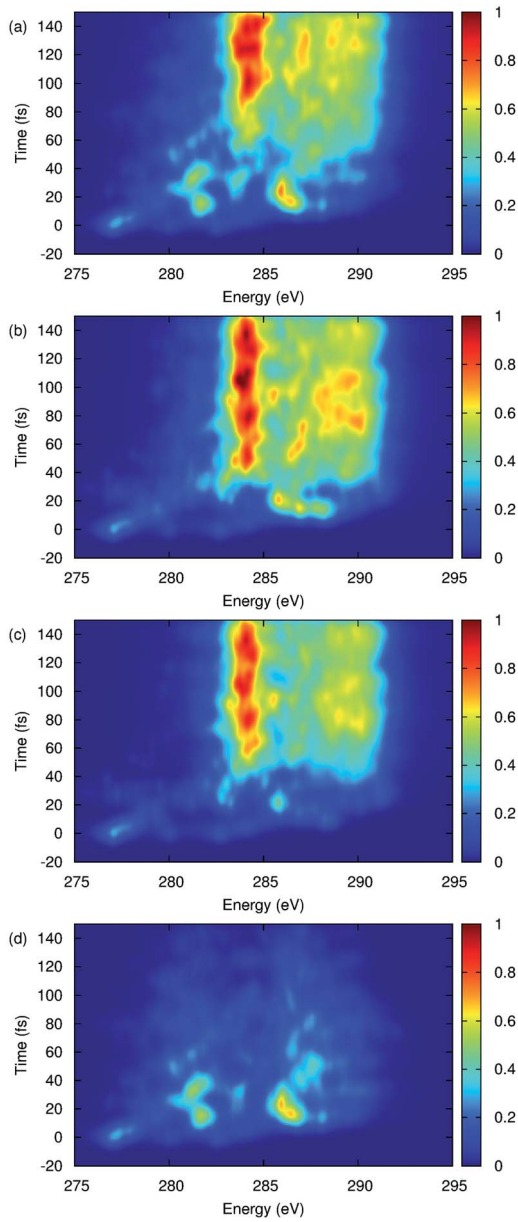

Fig. 8 Pre-edge TRXAS calculated using the results of AIMS simulations of ethylene excited to the $\pi\pi^*$ state. (a) TRXAS calculated with all states included; (b) TRXAS calculated from the valence-state-only AIMS calculation; (c) TRXAS calculated from the valence-state-only AIMS calculation, and with trajectories in the S_1 state close to the Tw-Py seam removed, and; (d) TRXAS calculated from the all-state AIMS calculations with the contributions from the S_0 state trajectories removed from the spectrum calculation.

of the S_0 state. Additionally, the time at which this broad feature appears in the TRXAS is coincident with a significant re-population of the S_0 state, as seen in the calculated adiabatic state populations of Fig. 4(a). This strongly indicates that this

part of the TRXAS arises predominantly from excitation from the 'hot' ground electronic state. Confirmation of this assignment comes from the calculation of the TRXAS using only the Gaussian basis functions associated with the excited electronic states. The resulting spectrum, shown in Fig. 8(d), shows that eliminating the S_0 state from the TRXAS calculation removes the majority of the intensity at times $t > 50$ fs, confirming that this part of the TRXAS spectrum arises predominantly from excitation from the 'hot' S_0 ground state.

3.4 Time-resolved photoelectron spectra

Although the main focus of this work is the calculation of the TRXAS of photoexcited ethylene, we also present here the calculated TRPES. The primary reason for doing so is to compare and contrast the TRXAS, which probes the core-level electrons, to a well established method which probes the valence electrons.

The TRPES was calculated using a probe photon energy of 18 eV, chosen so that states above the double ionization threshold are not included in the calculation. Using a previously calculated double ionization potential of 29.5 eV (ref. 58) and the vertical excitation energy of 8.13 eV for the $S_2(\pi\pi^*)$ state furnished by our ADC(2)/6-311++G** calculations, a probe photon energy of 18 eV should be sufficiently low to exclude any states lying above the double ionization threshold from the TRPES calculation.

Shown in Fig. 9(a) is the TRPES calculated following excitation to the $S_2(\pi\pi^*)$ state. At time $t = 0$, the TRPES is dominated by two weak features centred at binding energies of around 2.1 and 15.5 eV. These correspond, respectively, to ionization of the initially excited $S_2(\pi\pi^*)$ state to the $D_0(\pi)$ and $D_9(\pi^*)$ states. Rapidly, within 10 fs, two new features appear at binding energies of around 2.9 and 14.6 eV. These peaks are found to correspond to ionization from the $S_1(\pi 3s)$ state to the cation states correlating with the $D_0(\pi)$ and $D_5(\sigma)$ states at the FC point. That these peaks correspond to ionization from the transiently populated $\pi 3s$ state is seen most clearly in Fig. 9(b), which shows the TRPES calculated from the valence-state-only AIMS calculations. The removal of this state manifests itself in the TRPES as the vanishing of these two peaks. Additionally, the broader feature appearing at a binding energy of around 12.5 eV after $\sim$15 fs is also found to disappear, implying that this also corresponds to ionization from the $\pi 3s$ state. In agreement with previous work,[52] it can thus seen that the calculated TRPES contains signatures of internal conversion from the initially excited $\pi\pi^*$ state to the lower-lying $\pi 3s$ state.

The most intense feature in the calculated TRPES is the broad set of peaks appearing after about 50 fs at binding energies between 10 and 16 eV, corresponding to ionization from the repopulated S_0 ground state. This is confirmed by the TRPES calculated using only Gaussian basis functions associated with the excited electronic states, as shown in Fig. 9(d).

Finally, we investigate whether the calculated TRPES reveals the structural or electronic dynamics upon the approach to the dominant Tw-Py intersection seam in the $\pi\pi^*$ state. To do so, the TRPES was recalculated from AIMS calculation with the removal of the $\pi 3s$ state and all contributions from S_1-state Gaussian basis functions with a first-order distance $D_{12}(\bar{\mathbf{R}}_j^{(I)}; \mathbf{R}_{\text{Tw-Py}})$ from the Gaussian centre to the Tw-Py intersection seam of less than 0.3 Å. The resulting spectrum is shown in Fig. 9(c). This spectrum is compared to that shown in Fig. 9(b), which contains

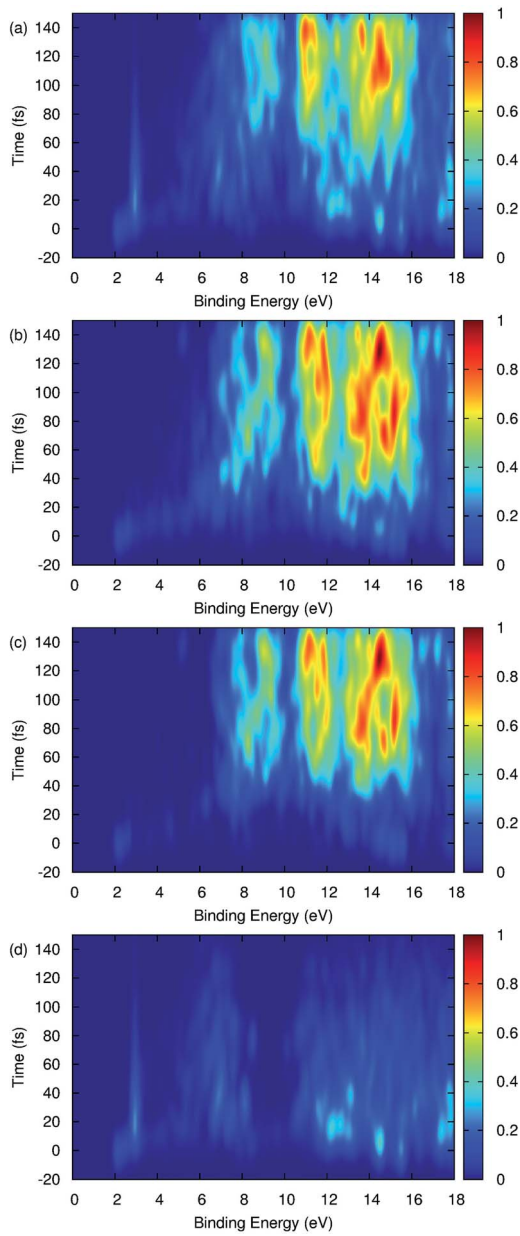

Fig. 9 Main features of TRPES estimated using the results of AIMS simulations of ethylene excited to the $\pi\pi^*$ state and a probe photon energy of 18 eV. (a) TRPES calculated with all states included in the AIMS calculation; (b) TRPES calculated from the valence-state-only AIMS calculation; (c) TRPES calculated using the valence-state-only AIMS calculation, and with trajectories in the S_1 state close to the Tw-Py seam removed, and; (d) TRPES calculated from the all-state AIMS calculations with the contributions from the S_0 state trajectories removed from the spectrum calculation.

contributions from the valence states only. Some small differences are seen. However, in contrast to the TRXAS, there appear to be no clear signatures in the calculated TRPES of those components of the wavepacket which are in close proximity to the Tw-Py intersection seam.

It should be noted that all the features of the TRPES discussed above are well-separated in both energy and time. As a result of this, our analysis does not rely on their relative intensities or the vibrational fine structure. Therefore, it remains valid despite the crudeness of the approximations adopted in the calculation of the model TRPES (see Section 2.2).

4 Discussion

The pre-edge part of the TRXAS calculated for ethylene following excitation to the $S_2(\pi\pi^*)$ state contains clear signatures of the most pertinent aspects of the ensuing excited state dynamics. Namely: (i) the initial large amplitude nuclear motion in the $\pi\pi^*$ state; (ii) the transient population of the π3s state; (iii) the re-population of the S_0 state, and; (iv) the movement of the wavepacket towards the vicinity of the Tw-Py conical intersection seam. It is important to note that the calculated TRPES also contains discernible information about the first three of these processes. However, the TRXAS is found to possess a level of clarity and ease of interpretation that surpasses that of the TRPES.

The main reason for the dynamical information encoded in the TRXAS being so clear is that the pre-edge XAS for the $\pi\pi^*$ and π3s states are dominated by a small number of core-to-valence transitions having rather large energetic separations. The TRPES, in contrast, is significantly more congested, with a comparatively larger number of less well resolved excited-state photoionization channels being open. Remarkably, only the TRXAS is predicted to contain a direct and clear signature of the arrival of the wavepacket at the Tw-Py intersection between the $\pi\pi^*$ and ground states. In subsections 4.1 and 4.2, we discuss the main reasons for these differences. Finally, in subsection 4.3 we offer some perspective on the potential generality of these results.

4.1 Discrimination between the dynamics in the $\pi\pi^*$ and π3s states

The main reason for the distinct clarity of the calculated TRXAS is that the $\pi\pi^*$ and π3s states are effectively projected by core-to-valence excitation onto disjoint sets of small numbers of final states having large energetic separations. In contrast, in the TRPES the excited states are each projected onto larger intersecting (in the mathematical sense) sets of final cation states, making the interpretation of the spectrum less straightforward.

In the course of the short-time dynamics directly following excitation, the valence $\pi\pi^*$ undergoes preferential core-to-valence excitation to the 1sπ^* state, whilst the Rydberg π3s state is excited preferentially to the 1s3s state. This can be interpreted as core-to-valence excitation being dominated in each case by excitation of a C 1s electron into the hole in the singly-occupied π orbital. The vertical energy difference at the FC point between the 1sπ^* and 1s3s states is much greater than that between the $\pi\pi^*$ and π3s states: 2.2 eV *versus* 0.8 eV at the ADC(2)/CVS-ADC(2)x levels of theory using the 6-311++G** basis. Insight into this large energetic separation of the 1sπ^* and 1s3s states may be gained by

considering the application of a one-particle, one-hole (1p1h) excitation operator $\hat{C}_{vc} = \hat{c}_v^\dagger \hat{c}_c$ to the correlated ground electronic state $|\Psi_0\rangle$ to yield the singly core-excited configuration $|\Psi_{vc}\rangle = \hat{C}_{vc}|\Psi_0\rangle$, where c indexes a core orbital and v a virtual valence orbital. By applying Rayleigh–Schrödinger perturbation theory through second-order within the core valence separation approximation, the core-excitation energy ΔE_{vc} obtained using the unperturbed 1p1h configuration $|\Psi_{vc}\rangle$ can be written as follows:[46,59]

$$\Delta E_{vc} = \varepsilon_v - \varepsilon_c + [2\langle cv|vc\rangle - \langle cv|cv\rangle] + U_{vc}^{(2)}(1p1h) + U_{vc}^{(2)}(2p2h) + R_{vc}^{(2)}. \quad (10)$$

Here, ε_p denotes the energy of the canonical Hartree–Fock orbital φ_p. The second-order terms $U_{vc}^{(2)}(1p1h)$, $U_{vc}^{(2)}(2p2h)$ and $R_{vc}^{(2)}$ describe the interaction of $|\Psi_{vc}\rangle$ with other 1p1h and 2p2h configurations, and the partial compensation of the 3p3h contributions with the ground state correlation energy, respectively. Of more interest to us is the first-order Coulomb term $J_{vc} = \langle cv|cv\rangle$, which effectively accounts for the stabilizing Coulomb interaction between the excited electron and the core-hole. Owing to the spatially compact nature of the core-level orbital φ_c, the Coulomb integral J_{vc} can be expected to be smaller for a more diffuse virtual orbital φ_v. It then follows that a core-excited state characterized by excitation into a valence-type orbital may be stabilized to a greater extent relative to a core-excited state characterized by excitation into a Rydberg-type orbital. This, coupled with the propensity for core-to-valence excitation to result in excitation from a core-level orbital into the lowest-lying singly-occupied valence orbital, suggests that pre-edge X-ray absorption may be a particularly useful probe of vibronically coupled dynamics occurring in energetically proximate valence and Rydberg states.

4.2 Signature of the arrival of the wavepacket at the Tw-Py conical intersection seam

A remarkable finding is that the calculated TRXAS contains a peak centred around 286 eV, with a delayed rise, that maps onto the $\pi\pi^*$ state components of the wavepacket which come into close proximity with the Tw-Py intersection seam. To shed more light on the nature of this spectral feature, we consider the calculated XAS for the $\pi\pi^*$ state at the Tw-Py geometry, shown in Fig. 10. The pre-edge part of the spectrum contains two dominant transitions. The lower energy peak corresponds to excitation of a core electron into the hole in the singly-occupied π orbital, forming the $1s\pi^*$ state. This peak thus maps onto the dominant transition from the $\pi\pi^*$ state seen in the FC region spectrum. The appearance of a second, higher-energy peak in the spectrum is linked to the localization – that occurs as the system approaches the Tw-Py seam – of the 1s orbitals about the now non-equivalent carbon atoms. At the FC point, the near-degenerate 1s orbitals are not localized on the carbon atoms, as dictated by the D_{2h} symmetry of the molecule. At the Tw-Py geometry, however, the 1s molecular orbitals become localized on the now non-equivalent carbon atoms. This is accompanied by a large splitting, $\sim$4.5 eV, of the 1s orbital energies. The higher-energy peak in the pre-edge XAS is found to correspond to excitation from the lower-energy 1s orbital localized on the carbon atom of the pyramidalized CH_2 group. This result highlights a unique feature of the pre-edge TRXAS. Namely, that changes in geometry and/or electronic structure localized around specific atomic centres may appear in the spectrum as changes in core-to-valence excitation energies. These in turn

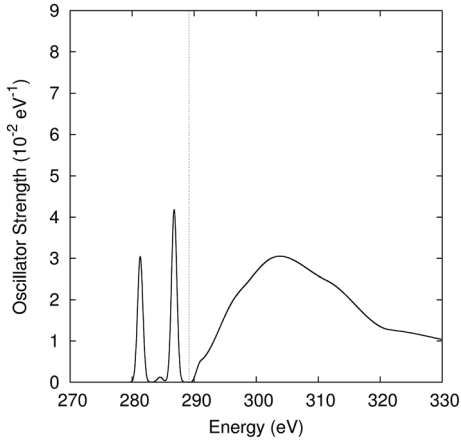

Fig. 10 Calculated XAS for the $\pi\pi^*$ state of ethylene at the Tw-Py conical intersection geometry. The initial valence-excited states are described at the ADC(2) level, and the final core-excited states at the CVS-ADC(2)x level. The dashed line marks the calculated C 1s ionization energy. The bound part of the spectrum was calculated using the 6-311++G** basis. The continuum part was calculated using the Stieltjes imaging technique with the cc-pVDZ basis augmented with 3s, 6p and 4d continuum-type KBJ functions.

result from corresponding changes in the energies of the atom-localized core orbitals.

4.3 Generality of the observed trends

We offer, for the purposes of this discussion, our perspective on the generality of the results presented here. Firstly, the excited-state dynamics of ethylene are characteristic of those of a large range of unsaturated hydrocarbons. To emphasize the idea that a chromophore such as the C=C bond acts as a dynamical moiety in larger systems, we have coined the term 'dynamophore'.[60] Accordingly, we expect that the results presented here will apply to related systems containing the C=C dynamophore. Secondly, and more broadly, we consider the predicted propensity for the excited-state, pre-edge XAS to be dominated by those core-to-valence transitions which correspond to the filling of the lowest-lying singly-occupied molecular orbital (SOMO) of the dominant electronic configuration characterizing the state being probed. As dictated by the one-electron nature of the dipole operator, core-to-valence excitation from an initial singly-valence-excited state should exhibit a propensity for excitation to a subset of core-excited states whose dominant configurations are related to that of the initial state by a single pair of orbital occupancies. It then seems reasonable that the lowest energy such transition may in general correspond to excitation of a core-level electron into the hole in the lowest-lying SOMO. Supporting this suggestion, we note that core-excitation into the singly-occupied molecular orbital is recognized as providing a unique fingerprint of radical species.[61] Informed by these two considerations, we propose that there is a propensity for the pre-edge XAS of a singly-valence-excited state to be dominated by the transition which fills the hole in the lowest lying SOMO.

5 Conclusions

Through the coupling of AIMS quantum dynamics calculations with CVS-ADC(2)x X-ray absorption cross-section calculations, a general and tractable method for the calculation of excited-state TRXAS spectra is presented. This methodology was applied to calculation of the TRXAS of ethylene excited to its $S_2(\pi\pi^*)$ state. In doing so, we identified features of TRXAS which make it a useful probe of ultrafast non-adiabatic dynamics. In particular, the pre-edge region of the XAS is predicted to exhibit pronounced sensitivity to the evolving electronic character of the excited-state wavepacket. The principal underlying reasons for this sensitivity are two-fold.

Firstly, we observed that core-to-valence excitation results in transition to a core-excited state which is related to the initial valence-excited state by the filling of the hole in the lowest lying SOMO. Therefore, the different valence-excited states are effectively projected onto distinct (and relatively sparse) sets of final states. As a result, the spectral features in the TRXAS which reflect the electronic dynamics can be well resolved.

Secondly, the high degree of localization of the core orbitals at non-symmetric nuclear geometries should allow for the potential identification of atom-localized changes in geometric and/or electronic structure. This is exemplified in the case of photo-excited ethylene by the prediction of two separate peaks in the TRXAS that map onto the arrival of the wavepacket at the Tw-Py CI seam, corresponding to excitation from the two energetically-split 1s orbitals localized on the now non-equivalent carbon atoms.

For comparison, the qualitative features of the TRPES of ethylene excited to its $S_2(\pi\pi^*)$ state were also estimated. By doing so, an insightful comparison between spectroscopies probing the core- *versus* valence-level electrons could be made. Both the calculated TRXAS and TRPES contain information about the electronic dynamics following excitation. However, this information seems to be encoded more clearly in the TRXAS. The primary reason for this is that, unlike core-to-valence excitation, valence-shell photoionization will generally project a given valence-excited state onto a large number of final (cation) states, leading to a higher density of overlapping spectral features in the TRPES. Additionally, due to the delocalized nature of the valence-level electrons, the atom-localized changes in geometric and electronic structure that appear clearly in the calculated TRXAS are absent from the TRPES.

The results presented here strongly suggest that the pre-edge region of the XAS is sensitive to both electronic and structural dynamics in photoexcited molecules. In particular, core-to-valence excitation provides clear discrimination between the components of the wavepacket associated with the different vibronically-coupled excited electronic states. In conclusion, we suggest that time-resolved pre-edge X-ray absorption spectroscopy will have significant potential as a spectroscopic probe of ultrafast excited state non-adiabatic dynamics.

6 Appendices

A Definition of the first-order seam distance

It is noted that first-order seam distance $D_{IJ}(\mathbf{R}; \mathbf{R}_{\mathrm{MECI}})$ may be written as:

$$D_{IJ}(\mathbf{R};\mathbf{R}_{\mathrm{MECI}}) = \left\{[\mathbf{P}_{IJ}(\mathbf{R}' - \mathbf{R}_{\mathrm{MECI}})]\cdot[\mathbf{P}_{IJ}(\mathbf{R}' - \mathbf{R}_{\mathrm{MECI}})]\right\}^{\frac{1}{2}}. \quad (11)$$

Here, $\mathbf{R}'$ denotes the geometry obtained after putting $\mathbf{R}$ into maximum coincidence with $\mathbf{R}_{\mathrm{MECI}}$ (in the least squares sense) *via* centre of mass translations, rotations, and the permutation of identical nuclei. The matrix $\mathbf{P}_{IJ}$ is the orthogonal projector onto the branching space for the MECI of interest:

$$\mathbf{P}_{IJ} = \sum_{i=1,2} \mathbf{x}_{IJ}^{(i)} \otimes \mathbf{x}_{IJ}^{(i)}, \quad (12)$$

where $\otimes$ denotes the outer product, and the $\mathbf{x}_{IJ}^{(i)}$ denote any two orthonormal vectors spanning the branching space. Specifically, we chose

$$\mathbf{x}_{IJ}^{(1)} = \frac{\mathbf{g}_{IJ}}{\|\mathbf{g}_{IJ}\|} \quad (13)$$

$$\mathbf{x}_{IJ}^{(2)} = \frac{\mathbf{h}_{IJ} - \left(\mathbf{h}_{IJ}\cdot\mathbf{x}_{IJ}^{(1)}\right)\mathbf{x}_{IJ}^{(1)}}{\left\|\mathbf{h}_{IJ} - \left(\mathbf{h}_{IJ}\cdot\mathbf{x}_{IJ}^{(1)}\right)\mathbf{x}_{IJ}^{(1)}\right\|}, \quad (14)$$

where $\mathbf{g}_{IJ}$ and $\mathbf{h}_{IJ}$ denote the gradient difference and non-adiabatic coupling vectors, respectively:

$$\mathbf{g}_{IJ} = \frac{\partial(E_J - E_I)}{\partial\mathbf{R}} \quad (15)$$

$$\mathbf{h}_{IJ} = \left\langle I\left|\left(\frac{\partial\hat{H}_{\mathrm{el}}}{\partial\mathbf{R}}\right)\right|J\right\rangle. \quad (16)$$

B Calculation of X-ray absorption spectra

The bound part of the spectrum, $\sigma_I^{(b)}(E;\mathbf{R})$, is calculated from the oscillator strengths $f_{IJ}(\mathbf{R})$ and vertical excitation energies ΔE_I^J between the initial valence-excited state $|I\rangle$ and the core-excited states $|J\rangle$ lying below the threshold for core-ionization:

$$\sigma^{(b)}(E;\mathbf{R}) = \left(\left[\sum_J f_{IJ}(\mathbf{R})\delta\left(E - \Delta E_I^J(\mathbf{R})\right)\right] * g(E;\eta)\right)\Theta(E_T(\mathbf{R}) - E). \quad (17)$$

Here, * denotes the convolution operation, $g(E;\eta)$ corresponding to a Gaussian function with full width at half maximum of η, and $\Theta(E_T - E)$ is the reverse Heaviside step function centred at the core-ionization threshold energy E_T. The free parameter η was chosen such that the broadening present in the experimental ground state XAS of a given system is incorporated into the calculated spectra.

Owing to the square integrable ($\mathscr{L}^2$) Gaussian basis sets used in our calculations, the cross-sections above the core-ionization threshold cannot be determined directly from the oscillator strengths for transition to the core-excited states $|J\rangle$ that lie within this domain. This arises from the different

normalizations of the $\mathscr{L}^2$ electronic states $|I\rangle$ and the 'true' continuum states $|E\rangle$: the former are normalized to a Kronecker-δ, $\langle I|J\rangle = \delta_{IJ}$, whilst the latter are energy normalized to a Dirac δ-function, $\langle E|E'\rangle = \delta(E - E')$. As such, a direct use of $\mathscr{L}^2$ states in the calculation of the oscillator strengths for excitation to states above the ionization threshold would lead to both incorrect values and incorrect dimensionalities. However, it is known to be possible to indirectly extract oscillator strengths corresponding to photo-ionization using an $\mathscr{L}^2$ basis *via* a procedure pioneered by Langhoff[39,40] and commonly referred to as Stieltjes imaging. The basis of the Stieltjes imaging method is the observation that the spectral moments $S_I(k)$ defined with respect to a given initial electronic state $|I\rangle$,

$$S_I(k) = \langle I|\hat{D}^\dagger \hat{H}^k \hat{D}|I\rangle, \tag{18}$$

can be accurately calculated *via* the insertion of the resolution of the identity expressed in terms of a given set $\{|\alpha\rangle\}$ of N-electron $\mathscr{L}^2$ basis functions:

$$S_I(k) = \sum_\alpha \langle I|\hat{D}^\dagger \hat{H}^k|\alpha\rangle\langle\alpha|\hat{D}|I\rangle = \sum_\alpha E_\alpha{}^k \left|\langle I|\hat{D}|\alpha\rangle\right|^2. \tag{19}$$

Equivalently, the resolution of the identity may be expressed in terms of the true bound and continuum states of the Hamiltonian, $\{|\iota\rangle\}$ and $\{|E\rangle\}$, respectively, giving

$$\begin{aligned} S_I(k) &= \sum_\iota E_\iota{}^k \left|\langle I|\hat{D}|\iota\rangle\right|^2 + \int_{E_T}^\infty E^k \left|\langle I|\hat{D}|E\rangle\right|^2 \mathrm{d}E \\ &= \sum_i E_\iota{}^k \left|\langle I|\hat{D}|\iota\rangle\right|^2 + \frac{3}{2}\int_{E_T}^\infty E^{k-1} f_I(E)\mathrm{d}E. \end{aligned} \tag{20}$$

From eqn (20), we see that $S_I(k)$ gives the kth moment of the photoabsorption cross-section. Then, by using the techniques of Stieltjes–Chebyshev moment theory, the photoabsorption cross-sections themselves may be extracted from a finite set of calculated spectral moments $S_I(k)$ evaluated using an $\mathscr{L}^2$ basis. In the work presented here, we follow the method outlined by Müller-Plathe and Diercksen.[62]

In the context of the present work, the $\mathscr{L}^2$ basis used in the expansion 19 of the spectral moments would be the CVS-ADC(2)x eigenstates. This approach, however, requires that the entire spectrum of the ADC Hamiltonian to be known, which is possible for only the smallest of systems. It has, however, recently been demonstrated that the spectral moments may be accurately and tractably approximated using the Lanczos pseudo-spectrum of the ADC Hamiltonan,[41–43] and it is this approach that is used in this work. In particular, we use the block variant of the Lanczos method[63,64] to generate the spectral moments $S_I(k)$ used in the Stieltjes imaging procedure.

C Calculation of ionization energies and Dyson orbitals

To calculate core-ionization energies, we make use of an idea from equation-of-motion coupled cluster theory whereby ionization to form an $(N-1)$-electron state is described in an N-electron framework by including an extremely diffuse

orbital in the one-electron basis and restricting the N-electron basis to span the subspace for which this 'continuum' orbital is occupied.[65] Accordingly, we calculate the energies of the singly core-ionized states within the N-electron ADC(2) framework by including a single uncontracted s-type orbital in the one-electron basis with an exponent of 10^{-30} and constructing the ADC Hamiltonian matrix in the space spanned by configurations that correspond to excitation of one, and only one core electron and for which only a single electron is excited into the extremely diffuse 'continuum' orbital. We term the resulting state the IP-ADC(2) state.

The Dyson orbital $\phi^{\mathrm{D}}_{I\alpha}$ for ionization from an N-electron state $|I\rangle$ to an $(N-1)$-electron state $|\alpha\rangle$ may be written in the second-quantization form

$$\phi^{\mathrm{D}}_{I\alpha} = \sum_p \langle \alpha | \hat{c}_p | I \rangle \varphi_{\mathrm{p}}, \tag{21}$$

where $\{\varphi_{\mathrm{p}}\}$ denotes the set of canonical Hartree–Fock orbitals. We now replace the true $(N-1)$-electron wavefunction $|\alpha\rangle$ in the expansion 21 by $\hat{c}_a|\bar{\alpha}\rangle$, where $|\bar{\alpha}\rangle$ denotes the corresponding N-electron IP-ADC(2) state and a indexes the diffuse 'continuum' orbital used in its construction. The resulting approximate formula for the Dyson orbital $\phi^{\mathrm{D}}_{I\alpha}$ reads

$$\phi^{\mathrm{D}}_{I\alpha} \approx \sum_p \langle \bar{\alpha} | \hat{c}^\dagger_a \hat{c}_p | I \rangle \varphi_{\mathrm{p}} = \sum_p \rho^{(\alpha I)}_{ap} \varphi_{\mathrm{p}}, \tag{22}$$

where $\rho^{(\alpha I)}$ denotes the transition density matrix between the IP-ADC(2) state $|\bar{\alpha}\rangle$, and the ADC(2) state $|I\rangle$. Eqn (22) represents our working equation for the calculation of approximate Dyson orbitals for core-ionization.

D Calculation of approximate overlaps between the ADC(2) and MR-FOCI states

In order to determine the initial ADC(2) state to be used in the calculation of the component spectra $\sigma^{(b/c)}_I(E; \bar{\mathbf{R}}^{(I)}_j(t))$ that are required for the computation of the TRXAS (see Section 2.3), approximate overlaps between the MR-FOCI states $|\Psi^{(\mathrm{CI})}_I\rangle$ of the AIMS calculations and the ADC(2) states $|\Psi^{(\mathrm{ADC})}_J\rangle$ at each Gaussian position $\bar{\mathbf{R}}^{(I)}_j(t)$ were calculated. The ADC state $|\Psi^{(\mathrm{ADC})}_J\rangle$ with the greatest absolute overlap value $|\langle \Psi^{(\mathrm{ADC})}_J | \Psi^{(\mathrm{CI})}_I \rangle|$ was then selected as the initial state in the X-ray absorption spectrum calculation.

Given the expansion of an MR-FOCI state $|\Psi^{(\mathrm{CI})}_i\rangle$ and an ADC(2) state $|\Psi^{(\mathrm{ADC})}_j\rangle$ in terms of Slater determinant bases $\{|k^{(\mathrm{CI})}\rangle\}$ and $\{|m^{(\mathrm{ADC})}\rangle\}$,

$$\left|\Psi^{(\mathrm{CI})}_i\right\rangle = \sum_k C^{(\mathrm{CI})}_{ki} \left|k^{(\mathrm{CI})}\right\rangle, \tag{23}$$

$$\left|\Psi^{(\mathrm{ADC})}_j\right\rangle = \sum_m C^{(\mathrm{ADC})}_{mj} \left|m^{(\mathrm{ADC})}\right\rangle, \tag{24}$$

the overlap integral $\langle \Psi^{(\mathrm{CI})}_i | \Psi^{(\mathrm{ADC})}_n \rangle$ may be straightforwardly calculated as

$$\left\langle \Psi^{(\mathrm{CI})}_i \middle| \Psi^{(\mathrm{ADC})}_j \right\rangle = \sum_{k,m} C^{(\mathrm{CI})*}_{ki} C^{(\mathrm{ADC})}_{mj} \det \mathbf{S}^{k^{(\mathrm{CI})}, m^{(\mathrm{ADC})}}. \tag{25}$$

Here, the $\mathbf{S}^{k(\mathrm{CI}),m(\mathrm{ADC})}$ denotes the matrix of overlaps between the molecular orbitals occupied in the determinants $|k^{(\mathrm{CI})}\rangle$ and $|m^{(\mathrm{ADC})}\rangle$.

The MR-FOCI states, which are expanded originally in a configuration state function basis, are easily re-expressed in the Slater determinant basis. The expression of the ADC(2) states in the Slater determinant basis is, however, non-trivial. Each ADC(2) state $|\Psi_j^{(\mathrm{ADC})}\rangle$ is expanded in terms of a basis $\{|\tilde{\Psi}_J\rangle\}$ of so-called intermediate states,

$$\left|\Psi_j^{(\mathrm{ADC})}\right\rangle = \sum_J X_{jJ}\left|\tilde{\Psi}_J\right\rangle. \tag{26}$$

The intermediate states $|\tilde{\Psi}_J\rangle$ are in turn constructed as orthonormalized linear combinations of the set of so-called correlated excited state $|\Psi_J^0\rangle$ defined by the operation of the physical excitation operators $\hat{C}_J^\dagger$ on the exact ground state wavefunction $|\Psi_0\rangle$:

$$|\Psi_J^0\rangle = \hat{C}_J^\dagger|\Psi_0\rangle, \tag{27}$$

$$\hat{C}_J^\dagger \in \{\hat{c}_a^\dagger\hat{c}_i;\ \hat{c}_a^\dagger\hat{c}_b^\dagger\hat{c}_i\hat{c}_j\ (a<b,\ i<j)\}, \tag{28}$$

where the $\hat{c}_p^\dagger$ and $\hat{c}_p$ denote the elementary creation and annihilation operators. To proceed, Møller–Plesset perturbation theory is used to provide a representation of the ground state wavefunction and energy:

$$|\Psi_0\rangle = |\Psi_0^{\mathrm{HF}}\rangle + |\Psi_0^{[1]}\rangle + |\Psi_0^{[2]}\rangle, \tag{29}$$

where $|\Psi_0^{\mathrm{HF}}\rangle$ denotes the Hartree–Fock ground state wavefunction and $|\Psi_0^{[i]}\rangle$ the ith-order correction to the Hartree–Fock wavefunction. The full expansions of the intermediate states are non-trivial to evaluate due to the appearance of n-particle density matrix elements of high values of n. As such, in the calculation of the overlaps $\langle\Psi_i^{(\mathrm{CI})}|\Psi_j^{(\mathrm{ADC})}\rangle$ we use only the zeroth-order expansions of the intermediate states,

$$|\tilde{\Psi}_{ai}\rangle \rightarrow |\tilde{\Psi}_{ai}^{(0)}\rangle = \hat{c}_a^\dagger\hat{c}_i|\Psi_0^{\mathrm{HF}}\rangle, \tag{30}$$

$$|\tilde{\Psi}_{aibj}\rangle \rightarrow |\tilde{\Psi}_{aibj}^{(0)}\rangle = \hat{c}_a^\dagger\hat{c}_b^\dagger\hat{c}_i\hat{c}_j|\Psi_0^{\mathrm{HF}}\rangle, \tag{31}$$

in conjunction with the expansion coefficients X_{jJ} furnished by the ADC(2) calculation employing the intermediate states to correct order. Although only approximate, this scheme is found to allow for a satisfactory matching of the ADC(2) states to corresponding MR-FOCI states, which is our principle requirement.

E AIMS calculations

In the AIMS simulations, the initial state used corresponds to vertical excitation from the ground state to the $S_2(\pi\pi^*)$ state. The initial positions and momenta were sampled using a Monte Carlo procedure from the ground state Wigner distribution. To do so, the harmonic approximation was employed, with the required frequencies and normal modes calculated at the CCSD(T)/cc-pVTZ level using the CFOUR program[66] program. Propagation times of 240 fs were used, with

time steps of 10 a.u. A total of 21 initial basis functions were used, with each being propagated independently, under the so-called independent first generation approximation.[37] Frozen Gaussian widths of 22.5 and 4.5 a.u. were used for the carbon and hydrogen atom coordinates, respectively.

Acknowledgements

AS and MS thank the NSERC Discovery grant program for financial support. VA acknowledges the financial support of the EPSRC through the programme grant on attosecond dynamics (EP/I032517/1).

References

1 A. Stolow, A. E. Bragg and D. M. Neumark, *Chem. Rev.*, 2004, **104**, 1719.
2 A. Stolow and J. G. Underwood, *Adv. Chem. Phys.*, 2008, **139**, 497.
3 J. Itatani, J. Levesque, D. Zeidler, H. Niikura, H. Pépin, J. C. Kieffer, P. B. Corkum and D. M. Villeneuve, *Nature*, 2004, **432**, 867.
4 O. Smirnova, Y. Mairesse, S. Patchkovskii, N. Dudovich, D. Villeneuve, P. Corkum and M. Y. Ivanov, *Nature*, 2009, **460**, 972.
5 W. Li, X. Zhou, R. Lock, S. Patchkovskii, A. Stolow, H. C. Kapteyn and M. M. Murnane, *Science*, 2008, **322**, 1207.
6 D. M. Jonas, *Annu. Rev. Phys. Chem.*, 2003, **54**, 425.
7 T. Brixner, J. Stenger, H. M. Vaswani, M. Cho, R. E. Blankenship and G. R. Fleming, *Nature*, 2005, **434**, 625.
8 M. Chergui, *Faraday Discuss.*, 2014, **171**, 11.
9 G. Sansone, L. Poletto and M. Nisoli, *Nat. Photonics*, 2011, **5**, 655.
10 F. Zamponi, Z. Ansari, M. Woerner and T. Elsaesser, *Opt. Express*, 2010, **18**, 947.
11 S. Khan, K. Holldack, T. Kachel, R. Mitzner and T. Quast, *Phys. Rev. Lett.*, 2006, **97**, 074801.
12 P. Beaud, S. L. Johnson, A. Streun, R. Abela, D. Abramsohn, D. Grolimund, F. Krasniqi, T. Schmidt, V. Schlott and G. Ingold, *Phys. Rev. Lett.*, 2007, **99**, 174801.
13 P. Emma, R. Akre, J. Arthur, R. Bionta, C. Bostedt, J. Bozek, A. Brachmann, P. Bucksbaum, R. Coffee, F. J. Decker, Y. Ding, D. Dowell, S. Edstrom, A. Fisher, J. Frisch, S. Gilevich, J. Hastings, G. Hays, P. Hering, Z. Huang, R. Iverson, H. Loos, M. Messerschmidt, A. Miahnahri, S. Moeller, H. D. Nuhn, G. Pile, D. Ratner, J. Rzepiela, D. Schultz, T. Smith, P. Stefan, H. Tompkins, J. Turner, J. Welch, W. White, J. Wu, G. Yocky and J. Galayda, *Nat. Photonics*, 2010, **4**, 641.
14 T. Ishikawa, H. Aoyagi, T. Asaka, Y. Asano, N. Azumi, T. Bizen, H. Ego, K. Fukami, T. Fukui, Y. Furukawa, S. Goto, H. Hanaki, T. Hara, T. Hasegawa, T. Hatsui, A. Higashiya, T. Hirono, N. Hosoda, M. Ishii, T. Inagaki, Y. Inubushi, T. Itoga, Y. Joti, M. Kago, T. Kameshima, H. Kimura, Y. Kirihara, A. Kiyomichi, T. Kobayashi, C. Kondo, T. Kudo, H. Maesaka, X. M. Marechal, T. Masuda, S. Matsubara, T. Matsumoto, T. Matsushita, S. Matsui, M. Nagasono, N. Nariyama, H. Ohashi, T. Ohata, T. Ohshima, S. Ono, Y. Otake, C. Saji, T. Sakurai, T. Sato, K. Sawada, T. Seike, K. Shirasawa, T. Sugimoto, S. Suzuki, S. Takahashi, H. Takebe,

K. Takeshita, K. Tamasaku, H. Tanaka, R. Tanaka, T. Tanaka, T. Togashi, K. Togawa, A. Tokuhisa, H. Tomizawa, K. Tono, S. K. Wu, M. Yabashi, M. Yamaga, A. Yamashita, K. Yanagida, C. Zhang, T. Shintake, H. Kitamura and N. Kumagai, *Nat. Photonics*, 2012, **6**, 540.

15 C. J. Milne, T. J. Penfold and M. Chergui, *Coord. Chem. Rev.*, 2014, **277–278**, 44.

16 C. Bressler and M. Chergui, *Chem. Rev.*, 2004, **104**, 1781.

17 Z. H. Loh, M. Khalil, R. E. Correa, R. Santra, C. Buth and S. R. Leone, *Phys. Rev. Lett.*, 2007, **98**, 143601.

18 C. La-O-Vorakiat, M. Siemens, M. M. Murnane, H. C. Kapteyn, S. Mathias, M. Aeschlimann, P. Grychtol, R. Adam, C. M. Schneider, J. M. Shaw, H. Nembach and T. J. Silva, *Phys. Rev. Lett.*, 2009, **103**, 257402.

19 L. X. Chen, *Annu. Rev. Phys. Chem.*, 2005, **56**, 221.

20 E. Goulielmakis, Z. H. Loh, A. Wirth, R. Santra, N. Rohringer, V. S. Yakovlev, S. Zherebtsov, T. Pfeifer, A. M. Azzeer, M. F. Kling, S. R. Leone and F. Krausz, *Nature*, 2010, **466**, 739.

21 W. Zhang, R. Alonso-Mori, U. Bergmann, C. Bressler, M. Chollet, A. Galler, W. Gawelda, R. G. Hadt, R. W. Hartsock, T. Kroll, K. S. Kjær, K. Kubiček, H. T. Lemke, H. W. Liang, D. A. Meyer, M. M. Nielsen, C. Purser, J. S. Robinson, E. I. Solomon, Z. Sun, D. Sokaras, T. B. van Driel, G. Vankó, T. C. Weng, D. Zhu and K. J. Gaffney, *Nature*, 2014, **509**, 345.

22 O. Gessner and M. Gühr, *Acc. Chem. Res.*, 2016, **49**, 138.

23 N. Huse, H. Cho, K. Hong, L. Jamula, F. M. F. de Groot, T. K. Kim, J. K. McCusker and R. W. Schoenlein, *J. Phys. Chem. Lett.*, 2011, **2**, 880.

24 B. Cooper, P. Kolorenč, L. J. Frasinski, V. Averbukh and J. P. Marangos, *Faraday Discuss.*, 2014, **171**, 93.

25 C. Bressler and M. Chergui, *Annu. Rev. Phys. Chem.*, 2010, **61**, 263.

26 F. de Groot, *Chem. Rev.*, 2001, **101**, 1779.

27 C. R. Natoli, M. Benfatto, S. D. Longa and K. Hatada, *J. Synchrotron Radiat.*, 2003, **10**, 26.

28 M. Benfatto and S. D. Longa, *J. Synchrotron Radiat.*, 2001, **8**, 1087.

29 T. Northey, N. Zotev and A. Kirrander, *J. Chem. Theory Comput.*, 2014, **10**, 4911.

30 A. Kirrander, K. Saita and D. V. Shalashilin, *J. Chem. Theory Comput.*, 2016, **12**, 957.

31 M. P. Minitti, J. M. Budarz, A. Kirrander, J. S. Robinson, D. Ratner, T. J. Lane, D. Zhu, J. M. Glowina, M. Kozina, H. T. Lemke, M. Sikorski, Y. Feng, S. Nelson, K. Saita, B. Stankus, T. Northey, J. B. Hastings and P. M. Weber, *Phys. Rev. Lett.*, 2015, **114**, 255501.

32 J. Stöhr, *NEXAFS Spectroscopy*, Springer, 1992.

33 A. R. Attar, A. Bhattacherjee and S. R. Leone, *J. Phys. Chem. Lett.*, 2015, **6**, 5072.

34 G. Capano, C. J. Milne, M. Chergui, U. Rothlisberger, I. Tavernelli and T. J. Penfold, *J. Phys. B: At. Mol. Phys.*, 2015, **48**, 214001.

35 G. Capano, M. Chergui, U. Rothlisberger, I. Tavernelli and T. J. Penfold, *J. Phys. Chem. A*, 2014, **118**, 9861.

36 G. Capano, T. J. Penfold, U. Rothlisberger and I. Tavernelli, *Chimia*, 2014, **68**, 227.

37 M. Ben-Nun and T. J. Martínez, *Adv. Chem. Phys.*, 2002, **121**, 439.

38 B. T. Pickup, *Chem. Phys.*, 1977, **19**, 193.

39 P. W. Langhoff, *Chem. Phys. Lett.*, 1973, **22**, 60.

40 P. Langhoff, C. T. Corcoran, J. S. Sims, F. Weinhold and R. M. Glover, *Phys. Rev. A*, 1976, **14**, 1042.
41 K. Gokhberg, V. Vysotskiy, L. S. Cederbaum, L. Storchi, F. Tarantelli and V. Averbukh, *J. Chem. Phys.*, 2009, **130**, 064104.
42 M. Ruberti, R. Yun, K. Gokhberg, S. Kopelke, L. S. Cederbaum, F. Tarantelli and V. Averbukh, *J. Chem. Phys.*, 2013, **139**, 144107.
43 M. Ruberti, R. Yun, K. Gokhberg, S. Kopelke, L. S. Cederbaum, F. Tarantelli and V. Averbukh, *J. Chem. Phys.*, 2014, **140**, 184107.
44 K. Pierloot, B. Dumez, P. O. Widmark and B. O. Roos, *Theor. Chim. Acta*, 1995, **90**, 87.
45 B. O. Roos, M. P. Fülscher, P. A. Malmqvist, M. Merchán and L. Serrano-Andrés, *Quantum Mechanical Electronic Structure Calculations with Chemical Accuracy*, Kluwer Academic Dordrecht, The Netherlands, 1995, p. 357.
46 J. Schirmer, *Phys. Rev. A*, 1982, **26**, 2395.
47 J. Schirmer, *Phys. Rev. A*, 1991, **43**, 4647.
48 J. Schirmer and A. Thiel, *J. Chem. Phys.*, 2001, **115**, 10621.
49 K. Kaufmann, W. Baumeister and M. Jungen, *J. Phys. B: At. Mol. Phys.*, 1989, **22**, 2223.
50 H. Lischka, R. Shepard, I. Shavitt, R. M. Pitzer, M. Dallos, T. MÃijller, P. G. Szalay, F. B. Brown, R. Ahlrichs, H. J. BÃűhm, A. Chang, D. C. Comeau, R. Gdanitz, H. Dachsel, C. Ehrhardt, M. Ernzerhof, P. HÃűchtl, S. Irle, G. Kedziora, T. Kovar, V. Parasuk, M. J. M. Pepper, P. Scharf, H. Schiffer, M. Schindler, M. SchÃijler, M. Seth, E. A. Stahlberg, J.-G. Zhao, S. Yabushita, Z. Zhang, M. Barbatti, S. Matsika, M. Schuurman, D. R. Yarkony, S. R. Brozell, E. V. Beck, J.-P. Blaudeau, M. Ruckenbauer, B. Sellner, F. Plasser and J. J. Szymczak, *Columbus, an ab initio electronic structure program, release 7.0*.
51 M. Schmidt, K. Baldridge, J. Boatz, S. Elbert, M. Gordon, J. Jensen, S. Kosecki, N. Matsunaga, K. Nguyen, S. J. Su, T. Windus, M. Dupuis and J. Montgomery, *J. Comput. Chem.*, 1993, **14**, 1347.
52 T. Mori, W. J. Glover, M. S. Schuurman and T. J. Martínez, *J. Phys. Chem. A*, 2012, **116**, 2808.
53 H. Tao, B. G. Levine and T. J. Martínez, *J. Phys. Chem. A*, 2009, **113**, 13656.
54 J. D. Coe, B. G. Levine and T. J. Martínez, *J. Phys. Chem. A*, 2007, **111**, 11310.
55 T. Kobayashi, T. Horio and T. Suzuki, *J. Phys. Chem. A*, 2015, **119**, 9518.
56 E. G. Champenois, N. H. Shivaram, T. W. Wright, C. S. Yang, A. Belkacem and J. P. Cryan, *J. Chem. Phys.*, 2016, **144**, 014303.
57 H. Tao, T. K. Allison, T. W. Wright, A. M. Stooke, C. Khurmi, J. van Tilborg, Y. Liu, R. W. Falcone, A. Belkacem and T. J. Martínez, *J. Chem. Phys.*, 2011, **134**, 244306.
58 E. Ohrendorf, H. Köppel, L. S. Cederbaum, F. Tarantelli and A. Sgamelloti, *J. Chem. Phys.*, 1989, **91**, 1734.
59 J. Schirmer, M. Braunstein, M. T. Lee and V. McKoy, *VUV and Soft X-Ray Photoionization*, Plenum Press, New York, 1996, ch. 4, p. 105.
60 O. Schalk, A. E. Boguslavskiy, A. Stolow and M. S. Schuurman, *J. Am. Chem. Soc.*, 2011, **133**, 16451.
61 M. Algia, M. Lavollée, R. Richter, U. Ekström, V. Carravetta, D. Stranges, B. Brunetti and S. Stranges, *Phys. Rev. A*, 2007, **76**, 022509.

62 F. Müller-Plathe and G. H. F. Diercksen, *Electronic Structure of Atoms, Molecules and Solids: II Brazilian School on Electronic Structure*, World Scientific, Singapore, 1990.
63 H. D. Meyer and S. Pal, *J. Chem. Phys.*, 1989, **91**, 6195.
64 B. N. Parlett, *The Symmetric Eigenvalue Problem*, Prentice-Hall, 1980, ch. 13.
65 J. F. Stanton and J. Gauss, *J. Chem. Phys.*, 1999, **111**, 8785.
66 J. F. Stanton, J. Gauss, M. E. Harding, P. G. Szalay, A. A. Auer, R. J. Bartlett, U. Benedikt, C. Berger, D. E. Bernholdt, Y. J. Bomble, L. Cheng, O. Christiansen, M. Heckert, O. Heun, C. Huber, T. C. Jagau, D. Jonsson, J. JusÃĬlius, K. Klein, W. J. Lauderdale, D. A. Matthews, T. Metzroth, L. A. MÃijck, D. P. O'Neill, D. R. Price, E. Prochnow, C. Puzzarini, K. Ruud, F. Schiffmann, W. Schwalbach, C. Simmons, S. Stopkowicz, A. Tajti, J. VÃązquez, F. Wang, and J. D. Watts, *Cfour, Coupled-cluster Techniques for Computational Chemistry, a Quantum-chemical Program Package*, see http://www.cfour.de.
67 R. McLaren, S. A. C. Clark, I. Ishii and A. P. Hitchcock, *Phys. Rev. A*, 1987, **36**, 1683.